Supplemental material of "Wave-kinetic dynamics of forced-dissipated turbulent internal gravity waves"

Vincent Labarre,[1,*] Giorgio Krstulovic,[1,†] and Sergey Nazarenko[2,‡]

[1] *Université Côte d'Azur, Observatoire de la Côte d'Azur, CNRS, Laboratoire Lagrange, Nice, France.*
[2] *Université Côte d'Azur, CNRS, Institut de Physique de Nice - INPHYNI, Nice, France*

This document gives technical details about the numerical resolution of the kinetic equation. Firstly, we describe the resonant manifold, the expression of the collision integral for axisymmetric and vertically symmetric spectra. Secondly, we show the numerical grids used for the computations. Thirdly, we present our integration and interpolation schemes. Finally, we explain our time-stepping scheme. The last sections provide additional studies based on wave kinetic equation simulations concerning the random perturbation of the initial condition and forcing shape and width.

COLLISION INTEGRAL AND RESONANT MANIFOLD

For axisymmetric and vertically symmetric spectra, the kinetic equation can be written as [1]

$$\dot{n}_{\boldsymbol{k}} = St_{\boldsymbol{k}}[n_{\boldsymbol{k}}] + \mathcal{F}_{\boldsymbol{k}} - \mathcal{D}_{\boldsymbol{k}} n_{\boldsymbol{k}} = 8\pi \int \left[\mathcal{R}_{12}^{\boldsymbol{k}(h)} - \mathcal{R}_{\boldsymbol{k}2}^{1(h)} - \mathcal{R}_{\boldsymbol{k}1}^{2(h)}\right] k_{1h} k_{2h}\, \mathrm{d}k_{1h} \mathrm{d}k_{2h} + \mathcal{F}_{\boldsymbol{k}} - \mathcal{D}_{\boldsymbol{k}} n_{\boldsymbol{k}} \tag{1}$$

$$\mathcal{R}_{12}^{\boldsymbol{k}(h)} = \frac{|V_{\boldsymbol{k}12}|^2}{|g'|\Delta}\ (n_1 n_2 - n_{\boldsymbol{k}} n_1 - n_{\boldsymbol{k}} n_2) \tag{2}$$

$$V_{\boldsymbol{k}12} = \sqrt{\frac{k_h k_{1h} k_{2h}}{32}} \left(\frac{\boldsymbol{k}_h \cdot \boldsymbol{k}_{1h}}{k_h k_{1h}} \sqrt{\left|\frac{k_{2z}}{k_z k_{1z}}\right|} + \frac{\boldsymbol{k}_h \cdot \boldsymbol{k}_{2h}}{k_h k_{2h}} \sqrt{\left|\frac{k_{1z}}{k_z k_{2z}}\right|} + \frac{\boldsymbol{k}_{1h} \cdot \boldsymbol{k}_{2h}}{k_{1h} k_{2h}} \sqrt{\left|\frac{k_z}{k_{1z} k_{2z}}\right|} \right) \tag{3}$$

$$\Delta = \frac{1}{2}\sqrt{(-k_h + k_{1h} + k_{2h})(k_h - k_{1h} + k_{2h})(k_h + k_{1h} - k_{2h})(k_h + k_{1h} + k_{2h})} \tag{4}$$

$$g' = \frac{k_{1h}\ \mathrm{sign}(k_{1z})}{k_{1z}^2} - \frac{k_{2h}\ \mathrm{sign}(k_{2z})}{k_{2z}^2} \tag{5}$$

where k_{1z}, k_{2z}, and the scalar products of horizontal wave-vectors ($\boldsymbol{k}_h \cdot \boldsymbol{k}_{1h}$, $\boldsymbol{k}_h \cdot \boldsymbol{k}_{2h}$, and $\boldsymbol{k}_{1h} \cdot \boldsymbol{k}_{2h}$) are evaluated for the solution of the resonance conditions, i.e. $\boldsymbol{k} = \boldsymbol{k}_1 + \boldsymbol{k}_2$ and $\omega_{\boldsymbol{k}} = \omega_1 + \omega_2$ (or permutations). Here, we have introduced a forcing term $\mathcal{F}_{\boldsymbol{k}}$ and dissipative term $\mathcal{D}_{\boldsymbol{k}} n_{\boldsymbol{k}}$, with $\mathcal{D}_{\boldsymbol{k}}$ a dissipation coefficient. We fix

$$\mathcal{D}_{\boldsymbol{k}} = \frac{1}{\omega_{\boldsymbol{k}}} \left[\left(\frac{k}{k_{\mathrm{d,sup}}}\right)^8 + \left(\frac{k_h}{k_{\mathrm{d,inf}}}\right)^{-8} + \left(\frac{|k_z|}{k_{\mathrm{d,inf}}}\right)^{-8} \right] \tag{6}$$

and

$$\mathcal{F}_{\boldsymbol{k}} = \frac{f_0}{\omega_{\boldsymbol{k}}} \exp\left[-\frac{(\ln k_h - \ln k_{\mathrm{f}h})^2 + (\ln |k_z| - \ln |k_{\mathrm{f}z}|)^2}{(\ln \Delta k_{\mathrm{f}})^2} \right], \tag{7}$$

were $(k_{\mathrm{f}h}, |k_{\mathrm{f}z}|)$ are the wave vectors component amplitudes of the forced modes, Δk_{f} fixes the width of the forcing, and the normalization factor f_0 is fixed such that the energy injection rate (computed numerically) is equal to unity.

The parametrization of the resonant manifold can be found in Lvov *et al.* [2]. For $\mathcal{R}_{12}^{\boldsymbol{k}(h)}$ $\boldsymbol{k} = \boldsymbol{k}_1 + \boldsymbol{k}_2$, $\omega_{\boldsymbol{k}} = \omega_1 + \omega_2$, we have the two branches

$$k_{1z} = \frac{k_z}{2k_h}\left(k_h + k_{1h} + k_{2h} + \sqrt{(k_h + k_{1h} + k_{2h})^2 - 4k_h k_{1h}}\right) \tag{8}$$

$$k_{1z} = \frac{k_z}{2k_h}\left(k_h - k_{1h} - k_{2h} - \sqrt{(k_h - k_{1h} - k_{2h})^2 + 4k_h k_{1h}}\right) \tag{9}$$

For $\mathcal{R}_{\boldsymbol{k}2}^{1(h)}$ $\boldsymbol{k}_1 = \boldsymbol{k} + \boldsymbol{k}_2$, $\omega_1 = \omega_{\boldsymbol{k}} + \omega_2$, we have the two branches

$$k_{1z} = \frac{k_z}{2k_h}\left(k_h + k_{1h} + k_{2h} - \sqrt{(k_h + k_{1h} + k_{2h})^2 - 4k_h k_{1h}}\right) \tag{10}$$

$$k_{1z} = \frac{k_z}{2k_h}\left(k_h - k_{1h} + k_{2h} - \sqrt{(-k_h + k_{1h} - k_{2h})^2 + 4k_h k_{1h}}\right) \tag{11}$$

The $\mathcal{R}^{2(h)}_{\boldsymbol{k}1}$ and $\mathcal{R}^{1(h)}_{\boldsymbol{k}2}$ terms give the same contribution to the collisional integral, which is used to reduce the computational cost. Because $(\boldsymbol{k}_h, \boldsymbol{k}_{1h}, \boldsymbol{k}_{2h})$ form a triad, they must satisfy the triangular inequalities

$$k_h \leq k_{1h} + k_{2h}, \quad k_{1h} \leq k_h + k_{2h}, \quad k_{2h} \leq k_{1h} + k_h, \tag{12}$$

meaning that (k_{1h}, k_{2h}) must lie in the so called "kinematic box" shown in Fig.1(a). It is therefore more convenient to work with the (p, q) variables such that

$$k_{1h} = \frac{k_h + p + q}{2} \quad \text{and} \quad k_{2h} = \frac{k_h - p + q}{2}. \tag{13}$$

The kinematic box is then given by the domain $(p, q) \in [-k_h, k_h] \times [0, \infty[$ and the collision integral reads

$$St_{\boldsymbol{k}} = 4\pi \int \left[\mathcal{R}^{\boldsymbol{k}(h)}_{12} - 2\mathcal{R}^{1(h)}_{\boldsymbol{k}2}\right] k_{1h} k_{2h} \, \mathrm{d}p\mathrm{d}q \tag{14}$$

and

$$\Delta(p, q) = \frac{1}{2}\sqrt{(k_h^2 - p^2)q(2k_h + q)}. \tag{15}$$

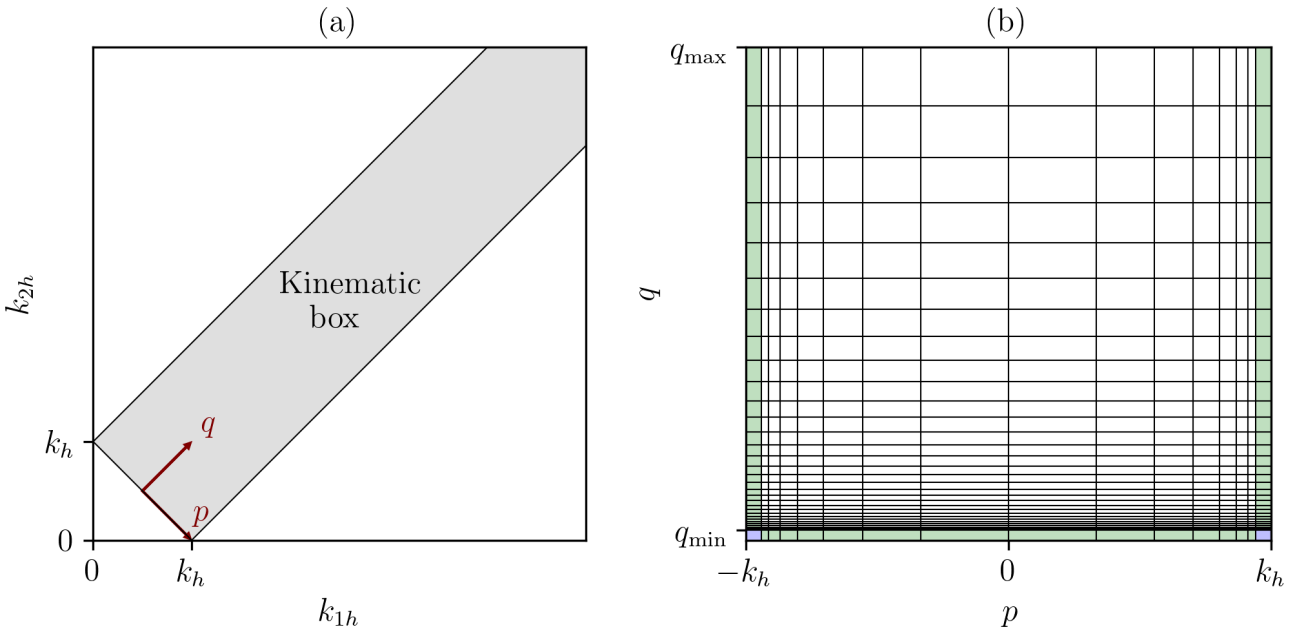

FIG. 1. (a) Kinematic box defined by conditions (12) and the (p, q) coordinates (13). (b) Illustration of the grid used for the computation of the collision integral at a given (k_h, k_z). Blue and green cells corresponds to regions where special treatment is required because of singularities (zeros of $\Delta(p, q)$). The size of these cells have been increased for visualization purposes.

NUMERICAL GRIDS

We store the spectra on a logarithmic grid of $M_h \times M_z$ points. Namely k_α takes values in

$$k_\alpha[i] = k_{\alpha,\max} \lambda_h^{-M_\alpha + i}, \quad i \in [1 : M_\alpha], \tag{16}$$

with $\lambda_\alpha = (k_{\alpha,\min}/k_{\alpha,\max})^{1/(1-M_\alpha)}$ for $\alpha = h$ or z. For each (k_h, k_z) of the grid, we compute $St_{\boldsymbol{k}}$ by integration over $(p, q) \in [-k_h, k_h] \times [0, q_{\max}]$, where $q_{\max} = 2k_{h,\max}$ is a cutt-off for large q (i.e. large k_{1h} and k_{2h}). We use logarithmic grids also for p and q: We note $p = \mp k_h \pm a$ where a takes value on a logarithmic grid of M_p points

between $a_{\min}$ and k_h (see equation (16)). To save computational time, we take $M_p = \max(8, i_h)$ where i_h is the k_h index on the (k_h, k_z) grid. For q, we use $M_q = 2M_h$ points grid between $q_{\min}$ and $q_{\max} = 2k_{h,\max}$. We choose $a_{\min} = k_{h,\min}/M_h$ and $q_{\min} = k_{h,\min}/M_q$ such that increasing resolution allows to improve accuracy at the border of the kinematic box. An illustration of the grid is given in Fig.1(b). With these choices, the numerical cost is $\sim M_h \times M_z \times M_p \times M_q \sim M_h^3 \times M_z$ operations per time step.

INTEGRATION AND INTERPOLATION SCHEMES

Integration on logarithmic grids are performed by using the trapezoidal rule after a change of variable. For example, integration in q gives

$$\int_{q_i}^{q_{i+1}} F(p,q)\ \mathrm{d}q = \int_{i}^{i+1} F(p,q)\ q \ln\lambda_q\ \mathrm{d}i \simeq \frac{F(p,q_i)q_i + F(p,q_{i+1})q_{i+1}}{2}\ \ln\lambda_q. \tag{17}$$

For $q \leq q_{\min} \ll k_{h,\min}$, we have an integrable singularity with $\Delta(p,q) \simeq \frac{1}{2}\sqrt{2(k_h^2 - p^2)\delta k_h^2}$ where $\delta = q/k_h \ll 1$, so the integration in q gives

$$\int_0^{q_{\min}} \frac{L(p,q)}{\Delta(p,q)}\ \mathrm{d}q \simeq \left(\frac{L(p,0) + L(p,q_{\min})}{\sqrt{k_h^2 - p^2}}\right)\ \sqrt{\frac{2q_{\min}}{k_h}}, \tag{18}$$

where the standard trapezoidal rule (without change of variable) is used and $L(p,0)$ is given by the maximum between 0 and a linear extrapolation. The contribution of the region $q \geq q_{\max}$ is not computed and is negligible because of dissipation. The integration scheme is easily adapted to the variable p, and generalized to 2D. We checked that this integration scheme allows us to reach order 2 precision. In order to compute $n_1 = (k_{1h}, |k_{1z}|)$ and $n_2 = (k_{2h}, |k_{2z}|)$, we interpolate with a bilinear fit of the form $n_{\boldsymbol{k}} = c_0 + c_h k_h + c_z|k_z| + \beta k_h|k_z|$, where (c_0, c_h, c_z, β) are constants in each cell. This interpolation scheme is of order 2 precision. For extrapolations, we simply fix $n_{\boldsymbol{k}}$ to the maximum between 0 and a linear fit whose coefficients are fixed with the two first grid points. We checked that the collision integral conserves well the energy for some test spectra. Namely, the energy conservation ratio $\int\ \omega_{\boldsymbol{k}} St_{\boldsymbol{k}}\ \mathrm{d}\boldsymbol{k} / \int\ \omega_{\boldsymbol{k}} |St_{\boldsymbol{k}}|\ \mathrm{d}\boldsymbol{k}$ (see Eden *et al.* [3]) remains less than few % in our simulations, and decreases as M^{-2} for $M = M_h = M_z$.

TIME STEPPING

For the time evolution, we use the splitting method. Namely, the dissipative operator is treated implicitly for half a time step. Then, we use the Runge-Kutta 2 method to treat the collision integral and forcing terms. Finally, we apply again the dissipation operator for half a time step. This method allows us to achieve second-order precision. We employ adaptative time-stepping to follow rapid changes in the wave-action spectrum, and to save computational time when slow changes occur. For this, we compute the ratio between the time step $\mathrm{d}t$ and the minimum of the nonlinear time $t_{\mathrm{nl},\boldsymbol{k}} = |n_{\boldsymbol{k}}/St_{\boldsymbol{k}}|$ (which is the inverse of the Boltzmann rate used in other studies, see e.g. [4]) every time step. If $\mathrm{d}t / \min_{\boldsymbol{k}} t_{\mathrm{nl},\boldsymbol{k}} > 0.5$, we decrease the time step by a factor 1.25. Conversely, if $\mathrm{d}t / \min_{\boldsymbol{k}} t_{\mathrm{nl},\boldsymbol{k}} < 0.05$, we increase the time step by a factor 1.25.

EFFECT OF RANDOM INITIAL CONDITION PERTURBATIONS

To check the influence of initial perturbations, we have run other simulations employing the log-normal forcing with $k_{\mathrm{f}h} = k_{\mathrm{f}z} = 0.07$, but with an initial perturbation for the wave-action spectrum:

$$n_{\boldsymbol{k}}(t=0) = \frac{a|\eta_{\boldsymbol{k}}|}{\omega_{\boldsymbol{k}}}, \tag{19}$$

where a is the noise amplitude and $\eta_{\boldsymbol{k}}$ is a random variable distributed according to the normal law. It corresponds to a statistically homogeneous perturbation of the 3D energy spectrum $n_{\boldsymbol{k}}\omega_{\boldsymbol{k}}$. For these simulations, we used $M_h =$

$M_z = 40$ grid points. In Fig.2, we show the 2D energy spectrum at different times for two simulations with $a = 0.01$ and $a = 1$. We observe that the same interactions (local and nonlocal) are responsible for the evolution of the energy spectrum. Yet, when the noise amplitude is larger, it takes a longer time to see the resonance lines emerge from the background noise (Fig.2(d)) when compared to a simulation with a small noise amplitude (Fig.3(b)). Interestingly, we see that the spectrum is smoothed out in regions near the nonlocal interactions branches toward large wave vectors, shown by dashed lines in Fig.2(c) and (f). It shows that the forcing can interact directly with small scales through non-local interactions. Yet, it does not significantly change the evolution of the internal gravity wave spectrum, at least for this set of parameters.

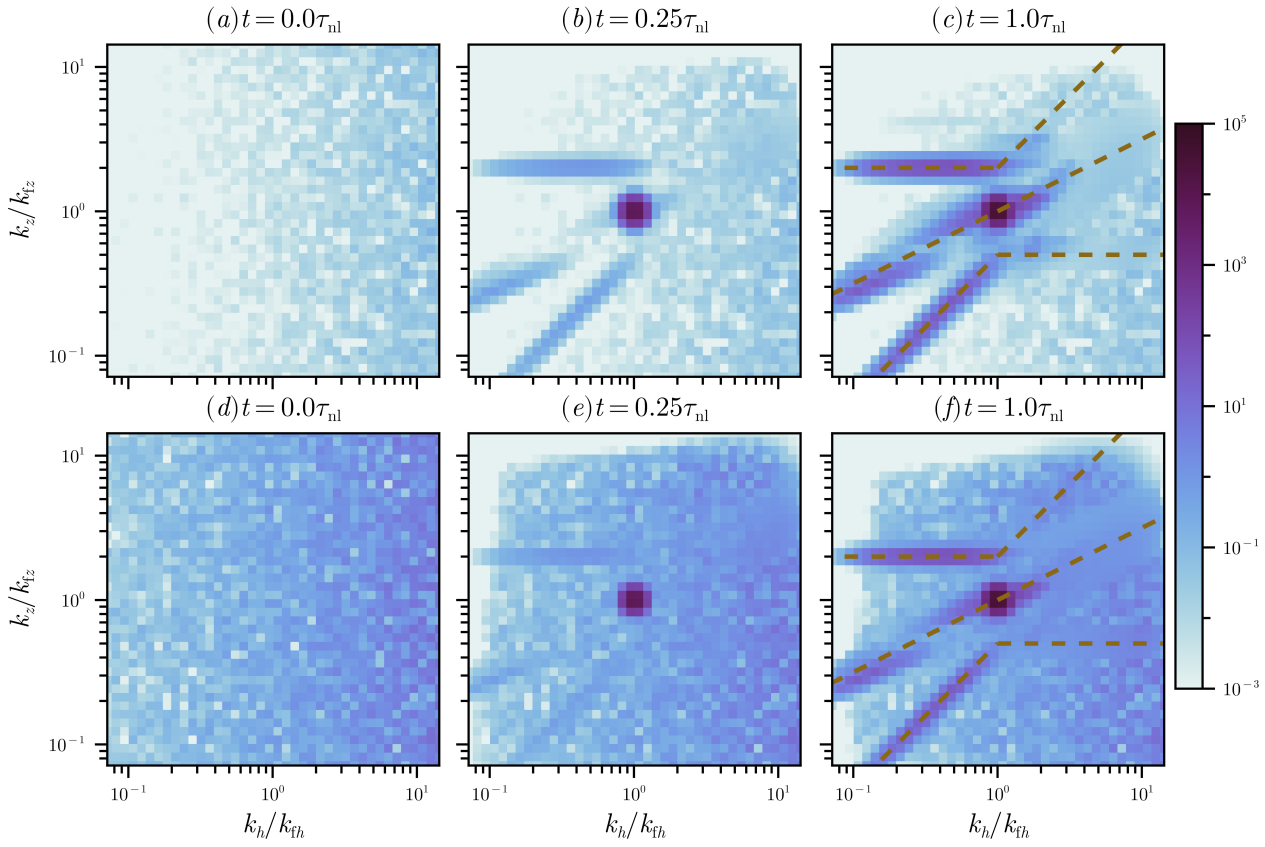

FIG. 2. 2D energy spectrum $e(k_h, k_z, t)$ at different times for two simulations with two different initial noise amplitude (19): (a-c) Small noise amplitude $a = 0.01$ and (d-f) Large noise amplitude $a = 1$. Dashed lines are for non local interactions (see Fig.2 of the manuscript).

EFFECT OF FORCING SHAPE AND WIDTH

To check the influence of the forcing properties, we have run other simulations employing a top-hat forcing:

$$\mathcal{F}_{\boldsymbol{k}} = \frac{f_0}{\omega_{\boldsymbol{k}}}\Theta(k_h - k_{\mathrm{f}h}/w)\Theta(k_h + k_{\mathrm{f}h}w)\Theta(k_z - k_{\mathrm{f}z}/w)\Theta(k_z + k_{\mathrm{f}z}w), \tag{20}$$

where Θ is the Heaviside function, $k_{fh} = k_{fz} = 0.07$ is the forcing position, w the forcing width factor, and f_0 is such that the total energy injection rate is equal to unity. For these simulations, we used $M_h = M_z = 40$ grid points. In Fig.3, we show the energy spectrum at different times for two simulations with $w = 1.25$ and $w = 2$. We observe that the same interactions (local and nonlocal) are responsible for the evolution of the energy spectrum. Yet, a larger forcing width involves more resonances, spreading energy faster at early times (Fig.3(d)), when compared to a simulation with a narrow forcing (Fig.3(b)). In particular, the direct energy transfer (to large wave vectors) is faster

with a wide forcing range. Interestingly, the last state of the energy spectrum is very similar for $w = 1.25$ (Fig.3(c)) and $w = 2$ (Fig.3(f)).

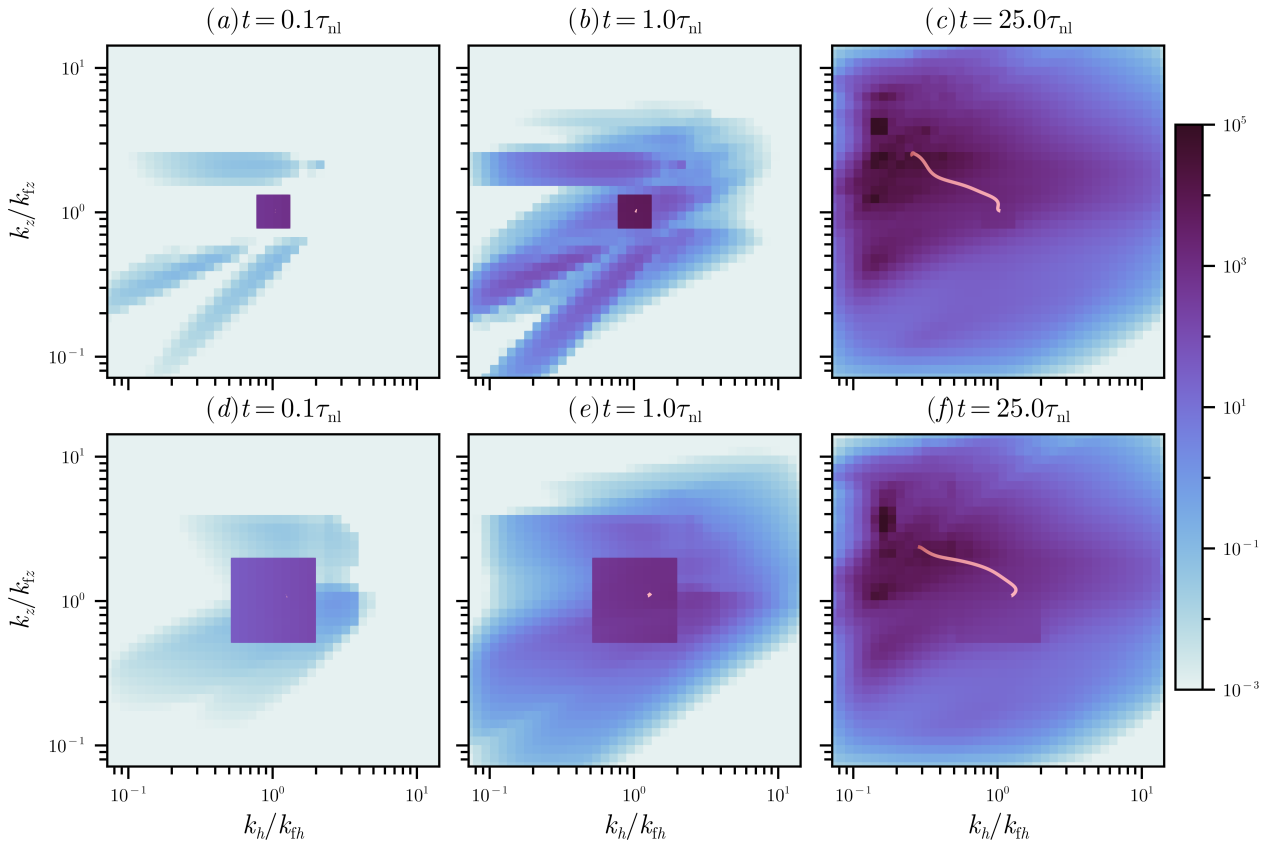

FIG. 3. 2D energy spectrum $e(k_h, k_z, t)$ at different times for two simulations with top-hat forcing with different width (20): (a-c) Small forcing width $w = 1.25$ and (d-f) Large forcing width $w = 2$. The colored lines shows the trajectory of the integral scales (see Fig.4 of the manuscript).

* vincent.labarre@oca.eu
† giorgio.krstulovic@oca.eu
‡ sergey.nazarenko@unice.fr

[1] G. Dematteis and Y. V. Lvov, Downscale energy fluxes in scale-invariant oceanic internal wave turbulence, Journal of Fluid Mechanics **915**, A129 (2021), publisher: Cambridge University Press.
[2] Y. V. Lvov, K. L. Polzin, E. G. Tabak, and N. Yokoyama, Oceanic internal-wave field: Theory of scale-invariant spectra, Journal of Physical Oceanography **40**, 2605 (2010).
[3] C. Eden, F. Pollmann, and D. Olbers, Numerical evaluation of energy transfers in internal gravity wave spectra of the ocean, Journal of Physical Oceanography **49**, 737 (2019).
[4] Y. V. Lvov, K. L. Polzin, and N. Yokoyama, Resonant and near-resonant internal wave interactions, Journal of Physical Oceanography **42**, 669 (2012).